CrystEngComm

Accepted Manuscript

ROYAL SOCIETY OF CHEMISTRY

www.rsc.org/crystengcomm

Enhanced Photoelectronic Properties by CdS Nanoparticles Selectively Deposited on {101} Facets of Single Crystal TiO_2 Nanosheet Array Films

Lei Yang,[a,b] Haiyan Jiang,[c] Weihua Wang,[b] Delin Chu,[b] Jinhong Yang,[b] Miao Zhang,[a] Jianguo Lv,[d] Baoming Wang,[b] Gang He,[a] and Zhaoqi Sun*[a]

[a] School of Physics & Material Science, Anhui University, Hefei 230601, PR China.

[b] Army officer academy, Hefei 230031, PR China.

[c] Hefei University of Technology Hefei 230009, PR China.

[d] School of Electronic & Information Engineering, Hefei Normal University, Hefei 230601, PR China.

Keywords:

TiO_2 nanosheet array {101} facets Selective deposition CdS nanoparticles Photoelectronic property

Abstract

Single crystal TiO_2 nanosheet array films with dominant {001} Facets were synthesized on FTO by a hydrothermal method. A simple strategy for the selective deposition of CdS nanoparticles on the low energy {101} facets by controlling F content on the surface of TiO_2 nanosheets is developed. For CdS/TiO_2, under light irradiation, the photo-generated electrons flow from {001} to {101} facets, meanwhile, the photo-generated electrons transfer from CdS nanoparticles to the TiO_2 nanosheets. The deposition of CdS nanoparticles on the {101} facets will shorten the path-ways that electron must travel. Herein, the synergistic effect of selective

deposition of CdS nanoparticles on the {101} facets of TiO_2 nanosheets combined with the different band edge positions of {001} and {101} facets, which would facilitate the spatial separation of electrons and holes on different facets, leading to enhanced photoelectronic performance.

1. Introduction

Recently, a series research groups have focused on the high energy {001} facet of anatase TiO_2 in order to accomplish efficient solar energy conversion and photocatalysis,[1-4] since Yang et al. reported the preparation of single crystal anatase TiO_2 nanosheets (TNS) with 47% exposed {001} facets.[5] In particular, single crystal anatase TNS grown directly on conducting substrates attract more attention,[6-8] because not only could they reduce inner defects and grain boundaries obviously compared with polycrystal films, but also each nanosheet contacts with the conductive substrate independently, and provides a direct pathway for charge transport.[9] However, due to its low absorption of solar light and fast recombination of photo-generated electron-hole pairs, the solar energy conversion of TNS is generally retarded. To solve this problem, a variety of strategies, including the doping of transition metals,[10,11] noble metals,[12-14] and semiconductors[15-18] have been developed.

Based on the spatial separation of reduction and oxidation sites on different facets of TiO_2, Ohno et al. observed the selective deposition of Pt and PbO_2 on rutile {110} and {011} facets.[19] Liu et al. reported selective deposition of Pt on {101} facets of anatase crystals showing a higher photocatalytic hydrogen evolution.[20] Besides, Ohno et al. also prepared selective deposition of Pt nanoparticles on the

inside surface of TiO_2 nanotube by washing with deionized water, and they found the active sites on the outside surface of TiO_2 nanotube were not covered by Pt nanoparticles, resulting in an increase in its photocatalytic activity.[21] For anatase TiO_2, it was proposed that the {001} facets show a higher surface energy than the {101} facets,[5,22-24] and their high surface energy induce high surface activities, which will make a stable combination with the foreign atoms.[25] Zhang et al. prepared TiO_2 single crystals with high energy {001} and {110} facets. They found the density of Au particles on {110} and {001} facet is larger than that on {101} facets, which would promote the separation of electron-hole pairs.[26] Liu et al. have synthesized CdS quantum dot-decorated TiO_2 nanocrystals with stepped {101} surface and observed highly hydrogen production rate under visible light irradiation.[27] Although many research have been made on selective deposition, however, there is few report on the selective deposition of CdS nanoparticles on low energy {101} facets of single crystal TNS films.

In this study, TNS films were fabricated by a simple hydrothermal method. Selective deposition of CdS nanoparticles on {101} facets of TNS films was performed by controlling the F content on the surface of TNS. Enhanced photoelectronic properties and the probable reasons were discussed. In addition, a model of charge separation among different crystal faces and CdS particles was proposed.

2. Experimental

2.1 Preparation of CdS/TNS films

All major chemicals were analytical grade and were used as received without further purification. TNS films were fabricated by a hydrothermal method similar to the method described by Zheng et al..[28] 0.5 mL of tetrabutyl titanate was mixed with 30 mL hydrochloric acid aqueous solution (5.2M). The mixture was stirred for 10 min before 0.25 g ammonium hexafluorotitanate was added into the solution, and stirred for another 30 min. Then, the solution was transferred in a Teflon-lined cylindrical autoclave in which a piece of fluorine-doped tin oxide (FTO) with the conductive side facing up. The Teflon-lined autoclave was kept at 170□ for 16 h. After cooling down to room temperature, the FTO substrates were taken out and rinsed with deionized water thoroughly and then dried at 80□.

Selective deposition of CdS nanoparticles on the TNS films was performed by successive ion-layer adsorption and reaction (SILAR) approach. In a typical procedure, TNS films were sequentially immersed in two different aqueous solutions for 5 mins, first in 0.5 M cadmium nitrate ($Cd(NO_3)_2$) and then in 0.5 M sodium sulfide (Na_2S). Between each immersion step, the films were rinsed with deionized (DI) water to remove excess ions and dried under a stream of nitrogen. This SILAR operation was repeated for 3, 5, 7, and 9 times, and they were denoted as CdS/TNS-3, CdS/TNS-5, CdS/TNS-7, and CdS/TNS-9, respectively.

2.2 Characterization

The crystal structure of the CdS/TNS films was checked by means of X-ray diffraction (XRD, MAC, M18XHF). The morphology was characterized by scanning electron microscopy (FE-SEM, Hitachi, S4800) and high-resolution transmission

electron microscopy (HRTEM, JEM-2100). X-ray photoelectron spectrometer (XPS, Thermo, ESCALAB250) was employed to analyze the elemental chemical status and surface composition of the samples. The amount of CdS in the prepared samples was measured by inductively coupled plasma atomic emission spectrometer (ICP-AES, IRIS Intrepid II XSP, Thermo Elemental). Absorbance spectra of the samples were obtained by an ultraviolet-visible spectrophotometer (UV-2550, Shimadzu). Photoluminescence (PL) spectra were measured by fluorescence spectrophotometer (FL, HITACHI F-4500) with the excitation wavelength of 325 nm under ambient conditions.

2.3 Photoelectronic performance measurements

Photoelectronic performance was measured by electrochemical workstation (CHI600D) in a photoelectron chemical cell under intermittent AM 1.5G simulated sunlight illumination with 0 V bias potential in 0.1 M Na_2SO_4 aqueous solution. In this system, Ag/AgCl (saturated with KCl), Pt foil and CdS/TNS films were used as the reference, counter and working electrodes, respectively. The distance between the sample and the counter electrode was 2 cm.

3. Results and discussion

3.1 XRD pattern

The experimental XRD patterns are shown in Fig. 1. The main characteristic peaks can be indexed to pure anatase phase (JCPDS no. 21-1272). Unlike the conventional method that preparing TiO_2,[29,30] the (004) diffraction peak here is significantly enhanced, indicating the exposing of large percentage of {001} facet.[28]

Compared with the obvious anatase phase, the diffraction peaks of CdS were not easily observed, implying its low content and the small size of CdS species.[31,32] For CdS/TNS-9, one can see that the diffraction peak at 26.5° is slightly intensified. It could be ascribed that characteristic peak corresponding to (002) plane of CdS (JCPDS No. 41-1049) was obscured by the FTO peak.

3.2 morphology analysis

Fig. 2(a) and (b) show the top view and cross-sectional view SEM images of a typical as-synthesized TNS on FTO substrate. Dense regular nanosheets with a side length of ~ 2 μm and a thickness of ~ 250 nm tend to grow vertically or obliquely on the FTO substrate. Fig. 2(c)-(d) show the magnified images of CdS/TNS-3, CdS/TNS-5, CdS/TNS-7 and CdS/TNS-9, respectively. From the symmetry of the well-faceted crystal structure of the TNS, the two flat square surfaces are identified as {001} facets, while the other lateral surfaces are {101} facets. With an increase in the number of deposition cycles, the surface of TNS become rough gradually. It is interesting to note that CdS nanoparticles are mostly selectively deposited on {101} facets of anatase TNS. As shown in Fig. 2(c), a small amount of CdS nanoparticles are deposited on the {101} facets of TNS after 3 deposition cycles. After 5 cycles, the amount of CdS nanoparticles increases obviously, with good dispersion on {101} facets. After 7 cycles, more CdS nanoparticles are deposited on the {101} facets, and agglomerate into larger particles. As shown in Table 1, the mean size of CdS nanoparticles decreases from 15.5 to 9.6 nm as the deposition cycles increase from 3 to 5 times, while with an increase in the number of deposition cycles from 5 to 9 times,

the mean size of CdS nanoparticles increases from 9.6 to 26.3 nm. As reported by Kamat et al.[33] there are two growth types of CdS nanocrystal with increasing deposition cycles. One is the formation of new crystallites, while the other is the growth of smaller crystallites into larger crystallites. As the deposition cycles increase to 5, it seems that the first type of growth hold the dominate position. After 5 deposition cycles, CdS crystallites grow into larger crystallites, resulting the increase of mean size of CdS nanoparticles.

Previously, it was proposed that for anatase single crystal, the {001} facets show a higher surface energy than the {101} facets. Their high surface energy induces high surface activity, which will make a strong combination with the foreign atoms such as CdS. In our experiment, the {101} facets of the samples are selectively deposited by CdS, which might due to the {001} and {101} facets were terminated by fluorine anions. For F-adsorbed surfaces, {001} facets become more stable than {101} facets. [5,34] To elucidate the role of fluorine anions in affecting the deposition of CdS, before deposition of CdS, a TNS film was annealed at 500□ for 2 h, and then prepared with 5 deposition cycles. From Fig. 3(b), it is worthwhile pointing out that the density of CdS particles on the {001} facets of TNS annealed at 500□ is higher than that on {101} facets. From EDS spectra, we can see that in addition to peaks from O, Ti, Cd, F and S, peaks from the C contamination and FTO substrate are also present. As shown in Fig. 3(c)-(f) and table 2, the mass percent of F element reduces from ~5.7 to ~2.6% after calcination, this is due to the adsorbed fluorine ions on the surface of TiO_2 can be removed by calcination[5]. Meanwhile, the mass percent of Cd element on

{101} and {001} facets for TNS unannealed are 1.13 and 0.61%, respectively. However, for TNS annealed at 500□, the mass percents of Cd element on {101} and {001} facets are 1.29 and 1.77%, respectively. A careful observation of the EDS spectra reveals that the density of CdS nanoparticles loaded on the {101} facets is much higher than that loaded on the {001} facets when their surface adsorbed more F^- anions. Besides, the density of CdS particles on TNS is obviously higher after calcination. This is because TNS films annealed at 500□ have a large percentage of {001} facets, which show higher surface energy and surface activity than {101} facets, that will make a strong combination with more CdS nanoparticles. In addition, the amount of Cd measured by ICP is 4.10 μg/cm^{-2} and 5.39 μg/cm^{-2} for the unannealed and annealed TNS films prepared with 5 deposition cycles.

3.3 TEM and HRTEM observation

The TEM image (Fig. 4(a)) of the CdS/TNS reveals that the TiO_2 nanosheets are rectangular-shaped structures, and their size is about 2 μm. The selected-area electron diffraction (SAED) of TNS (Fig. 4(b)) can be indexed as the [001] zone axis diffraction, which indicates that the top and bottom surfaces of the TiO_2 nanosheets are highly reactive {001} facets. Fig. 4(c) is the amplificatory image of {101} and {001} facets on CdS/TNS. Obviously, after 5 cycles, there are quite a few CdS particles deposited on the {101} facets, while fewer that is on {001} facets. The HRTEM image in Fig. 4(d) reveals a lattice fringe of about 0.237 nm, which corresponds to the (004) crystal plane of TiO_2, while d=0.316 nm corresponds to the (101) crystal plane of CdS, confirming the successful deposition of CdS on the {101}

facets of TNS.

3.4 XPS analysis

In order to investigate the chemical composition and elemental chemical status, XPS has been carried out for the as-synthesized unannealed and 500□ annealed TNS samples with 5 deposition cycles. Fig. 5(a) shows the comparison of survey spectra of the CdS/TNS. Sharp photoelectron peaks appear of Ti 2p, O 1s, Cd 3d and S 2p in both cases, along with a C 1s peak at 284.8 eV due to the adventitious hydrocarbon contamination or residual elements from precursor solution. Fig. 5(b) shows the comparison of high-resolution XPS spectra of the F 1s before and after annealing. As reported, F 1s peak at 684.5 eV originates from surface fluoride (Ti-F) formed by ligand exchange between F^- and surface -OH.[35] It is apparent that the surface fluoride of anatase single crystals can be removed by annealing method.[5] No signal at binding energy of 688.5 eV for F^- in the lattice of TiO_2 is found. Fig. 5(c) shows O 1s core level spectra which can be divided into three different peaks with binding energies at about 529.9, 531.5 and 532.6 eV. The former main peak at 529.9 eV is attributed to Ti-O in TiO_2 and the second peak can be assigned to the -OH on the surface of TiO_2.[36] Generally, the peak with binding energy at about 532.6 eV is attributed chemisorbed oxygen or organic carbon contaminations containing C-O species.[37-40] According to the results of curve fitting of O 1s spectra, hydroxyl content of the samples decreases form 31.6 to 29.9% after annealing, which is due to the dehydration reaction on the surface of the annealed TiO_2.[41] The S 2p spectra in Fig. 5(e) show obvious peaks at 161.5 and 162.6 eV, corresponding to the S $2p_{3/2}$ and S $2p_{1/2}$ of S 2p, the peak at about

169 eV is assigned to the formation of SO_4^{2-} or SO_3^{2-} species due to the oxidization of sulfide.[42,43] The binding energy of Ti $2p_{3/2}$ and Ti $2p_{1/2}$ is located at 458.7 and 464.5 eV. The peaks of Cd $3d_{5/2}$ and Cd $3d_{3/2}$ at 405.2 and 411.8 eV are all in good agreement with the previous studies.[44,45] The atomic ratio of Cd:S is 1.26:1 and 1.13:1 for the samples before and after annealing, which is expected for CdS nanoparticles under normal synthesis conditions.[42,46] In addition, it was found that the peak intensities for Cd 3d increase significantly after calcination, which is in good agreement with the findings of SEM and EDS. Meanwhile, the mean size of CdS nanoparticles in our experiment is approximate 10 nm, which is slightly larger than the depth that XPS could detect, thus, the decreasing for peak intensities of Ti 2p can be attributed to the increasing of CdS surface coverage.

3.5 UV-Visible absorption spectra

Fig. 6 presents typical absorption spectra of TNS films with different SILAR cycles. As shown, with an increase in the number of deposition cycles, the absorbance increases in the wavelength range from 400 to 500 nm. This can be attributed to the increase in the amount of CdS, which has a band gap bout 2.4 eV.[47] Based on the UV-Visible absorption spectra, the $(\alpha h\nu)^2$ vs photon energy plot of the films are shown in Fig. 7 and table 1. It can be seen that the adsorption bands of CdS/TNS show little variation, which changing from 3.21 to 3.16 eV. As reported by Zhang,[46] with an increase in the number of deposition cycles from 0 to 5 times, the band gap of CdS sensitized TiO_2 nanotube arrays shifts from 3.09 to 2.81 eV. Hu et al. reported that the absorption edge of the CdS sensitized TiO_2 nanorods shifts from 3.26 to 2.41

eV.[48] In our case, the CdS nanoparticles are mostly selectively deposited on {101} facets of TNS, resulting a low content of CdS and little change of adsorption bands.

3.6 PL spectra

For semiconductors, the PL spectrum is related to the trapping, immigration, and transfer of the photo-induced electrons and holes, so that it can reflect the separation and recombination of photo-induced charge carriers.[49,50] The PL spectra of TNS prepared with different SILAR cycles were obtained by using an excitation wavelength of 325 nm at room temperature. Three main peaks can be observed, which are situated at 397, 452 and 469 nm. The first peak is ascribed to the emission of band gap transition.[51] The emission peaks at 452 and 469 nm resulting from the oxygen defects, which is related to the charge-transfer transition from Ti^{3+} to oxygen anion in a TiO_6^{8-} complex.[51,52] Compared with bare TNS, the PL intensities of the CdS/TNS significantly decrease, indicating that CdS/TNS have lower recombination rate of photo-induced charge carriers. A observation of the PL spectra reveals that the PL intensity of CdS/TNS decreases with an increase in the number of deposition cycles from 3 to 7 times, indicating that the more CdS nanocrystallites are deposited on TNS {101} facets, the slower electron-hole pairs recombination. For CdS/TNS-9, the increase in PL intensity could be attributed to the aggregation of CdS nanoparticles. Furthermore, the intensity ratio of the band edge emission to visible emission decreases with increase in SILAR cycles, indicating that the oxygen defects of CdS/TNS increase with more CdS nanocrystallites are deposited on TNS.[53]

3.7 Transient photocurrent response

Fig. 9 shows the time-dependent photocurrent curves of CdS/TNS under intermittent AM 1.5G simulated sunlight illumination. As shown, the photocurrents increase with more SILAR cycles. After 7 cycles, the sample shows the biggest photocurrent value of ~60 μA/cm^2, which is about 10 times higher than that of the pristine TNS, nevertheless, it decreases as the deposition cycles increase to 9 times. The increase of photocurrent may be attributed to that CdS is a narrow band gap semiconductor, which would enhance absorbing of visible light. When the deposition cycles further increase to 9 times, the aggregation of CdS covering on the {101} facets of CdS/TNS-9, which leads to larger CdS particles. These large CdS particles might reduce the electron transfer rate.[54] Besides, the grain boundaries and defects among excess CdS nanoparticles can act as recombination center of charge carrier, which will result in the decrease in photoelectric performance.[9] Furthermore, from SEM images, it can be seen that {101} facets of CdS/TNS-9 are covered with CdS particles completely, which may inhibit the transfer of photoexcited electrons from the {001} facet to the {101} facet, resulting in the reduced photocurrent.

Fig. 10 is the schematic diagram of charge separation among different crystal faces and CdS particles. For F-adsorbed surfaces, it was proposed that Ti-F bonds are stronger in the {001} facets than that in the {101} facets, which induces the surface energy of {001} facet lower than that of {101} facets.[5] Recently, Ma et al. reported that the Ti-O bonds in the F-adsorbed {101} facets are weakened while strengthened in the {001} facets, so that {101} facets become more active than {001} facet, which will facilitate to make a strong combination with the foreign atoms such as CdS.[34]

Under light irradiation, the photo-excited electrons from the CdS can easily transfer to the {101} facets of TNS, due to the well-crystallized of TNS and the favorable energy level between CdS and TiO_2, thus prevent the recombination of electron-hole pairs.[55] Owing to the atomic arrangements characteristic, different crystal faces possess different surface band structures and band edge positions.[56] For anatase TiO_2, Ohno et al. found that the reduction and oxidation sites are located on {101} and {001} facets, respectively.[57] By means of single-molecule fluorescence spectroscopy, Tachikawa et al. demonstrated that electron flow from {001} to {101} facets.[58] Based on the density functional theory calculations, Yu et al. proposed a "surface heterojunction" concept to explain the difference in the photocatalytic activity of TiO_2 with coexposed {001} and {101} facets.[59] When CdS is combined with TiO_2, local band bending occurs at the CdS/TiO_2 interface. Under light irradiation, CdS effectively excites electron-hole pairs. The excited electrons can quickly transfer from the CdS conduction band to the TNS. Due to the converging of electron on {101} facets, the deposition of CdS particles on the {101} facets will shorten the path-ways that electron must travel, hence enable improve the separation of electrons and holes. Herein, enhanced photoelectronic performance of the CdS/TNS can be attributed to the synergistic effect of selective deposition of CdS nanoparticles on the {101} facets of TiO_2 nanosheets combined with the different band edge positions of {001} and {101} facets, which would facilitate the spatial separation of electrons and holes on different facets and retard the recombination of light generated electron-hole pairs.

4 Conclusions

In summary, we have developed a simple strategy for the selective deposition of CdS particles on the {101} facets by control the F content on the surface of TNS. For anatase single crystal, the electrons flow from {001} to {101} facets, the deposition of CdS nanoparticles on the {101} facets will shorten the path-ways that electron must travel, hence enable improve the separation of electrons and holes. The finding of this work provides a new way to improve photoelectronic performance through deposition of foreign atoms on the low energy surfaces.

Acknowledgements

This work is supported by the National Natural Science Foundation of China (Nos. 51472003 and 51272001), and the National Key Basic Research Program (2013CB632705), The authors would like to thank Yonglong Zhuang and Zhongqing Lin of the Experimental Technology Center of Anhui University, for the electron microscope test and discussion.

References

1. B. Banerjee, V. Amoli, A. Maurya, A. K. Sinha and A. Bhaumik, *Nanoscale*, 2015, 7, 10504-10512.
2. F. Wang, S. Zhang, C. Li, J. Liu, S. He, Y. Zhao, H. Yan, M. Wei, D. G. Evans and X. Duan, *RSC Adv.*, 2014, 4, 10834-10840.
3. B. Wang, X.-Y. Lu, L. K. Yu, J. Xuan, M. K. H. Leung and H. Guo, *CrystEngComm*, 2014, 16, 10046-10055.
4. Q. Shi, Y. Li, E. Zhan, N. Ta and W. Shen, *CrystEngComm*, 2015, 17, 3376-3382.
5. H. G. Yang, C. H. Sun, S. Z. Qiao, J. Zou, G. Liu, S. C. Smith, H. M. Cheng and G. Q. Lu, *Nature*, 2008, 453, 638-641.
6. F. Li, X. Li, R. Peng, X. Zhai, S. Yang, Z. Fu and Y. Lu, *Nanoscale*, 2014, 6, 12434-12439.
7. B. Liu and E. S. Aydil, *Chem. Commun.*, 2011, 47, 9507-9509.
8. T. K. Van, C. K. Nguyen and Y. S. Kang, *Chem.- Eur. J.*, 2013, 19, 9376-9380.
9. M. Zhou, X. W. D. Lou and Y. Xie, *Nano Today*, 2013, 8, 598-618.
10. M. Anpo and M. Takeuchi, *J. Catal.*, 2003, 216, 505-516.
11. J. Choi, H. Park and M. R. Hoffmann, *J. Phys. Chem. C*, 2009, 114, 783-792.
12. S. Zhu, S. Liang, Q. Gu, L. Xie, J. Wang, Z. Ding and P. Liu, *Appl. Catal. B*, 2012, 119, 146-155.
13. X.-F. Wu, Y.-F. Chen, J.-M. Yoon and Y.-T. Yu, *Mater. Lett.*, 2010, 64, 2208-2210.
14. D. Yang, N. Yang and J. Ge, *CrystEngComm*, 2013, 15, 7230-7235.
15. J. Hou, C. Yang, Z. Wang, S. Jiao and H. Zhu, *Appl. Catal. B*, 2013, 129, 333-341.
16. S. Lee, K. Lee, W. D. Kim, S. Lee, D. J. Shin and D. C. Lee, *J. Phys. Chem. C*, 2014, 118, 23627-23634.
17. X. Li, X. Chen, H. Niu, X. Han, T. Zhang, J. Liu, H. Lin and F. Qu, *J. Colloid Interface Sci.*, 2015, 452, 89-97.
18. Y. Zhu, R. Wang, W. Zhang, H. Ge and L. Li, *Appl. Surf. Sci.*, 2014, 315, 149-153.
19. T. Ohno, K. Sarukawa and M. Matsumura, *New J. Chem.*, 2002, 26, 1167-1170.
20. C. Liu, X. Han, S. Xie, Q. Kuang, X. Wang, M. Jin, Z. Xie and L. Zheng, *Chem. Asian J*, 2013, 8, 282-289.
21. K. Nishijima, T. Fukahori, N. Murakami, T.-a. Kamai, T. Tsubota and T. Ohno, *Appl. Catal. A*, 2008, 337, 105-109.
22. U. Diebold, *Surf. Sci. Rep.*, 2003, 48, 53-229.
23. T. Sun, Y. Wang, M. Al-Mamun, H. Zhang, P. Liu and H. Zhao, *RSC Adv.*, 2015, 5, 12860-12865.
24. C. Li, C. Koenigsmann, W. Ding, B. Rudshteyn, K. R. Yang, K. P. Regan, S. J. Konezny, V. S. Batista, G. W. Brudvig, C. A. Schmuttenmaer and J.-H. Kim, *J. Am. Chem. Soc.*, 2015, 137, 1520-1529.
25. D. He, M. Chen, F. Teng, G. Li, H. Shi, J. Wang, M. Xu, T. Lu, X. Ji, Y. Lv and Y. Zhu, *Superlattices Microstruct.*, 2012, 51, 799-808.
26. M.-Y. Xing, B.-X. Yang, H. Yu, B.-Z. Tian, S. Bagwasi, J.-L. Zhang and X.-Q. Gong, *J. Phys. Chem. Lett.*, 2013, 4, 3910-3917.
27. X. Yao, T. Liu, X. Liu and L. Lu, *Chem. Eng. J.*, 2014, 255, 28-39.
28. Z. Zheng, W. Xie, Z. S. Lim, L. You and J. Wang, *Sci. Rep.*, 2014, 4.
29. Y. Xu, M. Zhang, M. Zhang, J. Lv, X. Jiang, G. He, X. Song and Z. Sun, *Appl. Surf. Sci.*, 2014, 315, 299-306.

30. F. Meng, X. Song and Z. Sun, *Vacuum*, 2009, 83, 1147-1151.
31. Z. Bian, J. Zhu, S. Wang, Y. Cao, X. Qian and H. Li, *J. Phys. Chem. C*, 2008, 112, 6258-6262.
32. Y. Yang, J. Wen, J. Wei, R. Xiong, J. Shi and C. Pan, *ACS Appl. Mater. Interfaces*, 2013, 5, 6201-6207.
33. D. R. Baker and P. V. Kamat, *Adv. Funct. Mater.*, 2009, 19, 805-811.
34. X. Ma, Y. Dai, W. Wei, B. Huang and M.-H. Whangbo, *J. Phys. Chem. Lett.*, 2015, 6, 1876-1882.
35. K. Lv, Q. Xiang and J. Yu, *Appl. Catal. B*, 2011, 104, 275-281.
36. B. Gao, X. Yuan, P. Lu, B. Lin and Y. Chen, *J. Phys. Chem. Solids*, 2015, 87, 171-176.
37. E. Mccafferty and J. P. Wightman, *Surf.* Interface *Anal.*, 1998, 26, 549-564.
38. H. Liu, W. Yang, Y. Ma, Y. Cao, J. Yao, J. Zhang and T. Hu, *Langmuir*, 2003, 19, 3001-3005.
39. N. Kruse and S. Chenakin, *Appl. Catal. A*, 2011, 391, 367–376.
40. M. Zhang, M. Zhang, S. Shi, X. Song and Z. Sun, *J Alloy. Compd.*, 2014, 591, 213–217.
41. J. Yu, G. Dai and B. Cheng, *J. Phys. Chem. C*, 2010, 114, 19378-19385.
42. S. Chen, P. Maggie, R. Chuanmin, G. K. Mor, O. K. Varghese, K. Dimitris and C. A. Grimes, *J Photoch. Photobio. A*, 2006, 177, 177-184.
43. X. Wang, Z. Chen, Y. Luo, L. Jiang and R. Wang, *Sci. Rep.*, 2013, 3, 449-449.
44. S. Yousefzadeh, M. Faraji, Y. T. Nien and A. Z. Moshfegh, *Appl. Surf. Sci.*, 2014, 320, 772-779.
45. Y. Zhu, Y. Wang, Z. Chen, L. Qin, L. Yang, L. Zhu, P. Tang, T. Gao, Y. Huang, Z. Sha and G. Tang, *Appl. Catal. A*, 2015, 498, 159-166.
46. M. Zhang, S. Shi, G. He, X. Song and Z. Sun, *Sci. Adv. Mater.*, 2014, 6, 171-177.
47. N. Qin, Y. Liu, W. Wu, L. Shen, X. Chen, Z. Li and L. Wu, *Langmuir*, 2015, 31, 1203-1209.
48. Y. Hu, B. Wang, J. Zhang, T. Wang, R. Liu, J. Zhang, X. Wang and H. Wang, *Nanoscale Res. Lett.*, 2013, 8, 222.
49. J. Hou, C. Yang, Z. Wang, S. Jiao and H. Zhu, *Appl. Catal. B*, 2013, 129, 333-341.
50. Y. Wang, W. Chu, S. Wang, Z. Li, Y. Zeng, S. Yan and Y. Sun, *ACS Appl. Mater. Interfaces*, 2014, 6, 20197-20204.
51. F. B. Li and X. Z. Li, *Chemosphere*, 2002, 48, 1103-1111.
52. J.-G. Yu, H.-G. Yu, B. Cheng, X.-J. Zhao, J. C. Yu and W.-K. Ho, *J. Phys. Chem. B*, 2003, 107, 13871-13879.
53. J. Lv, W. Gong, K. Huang, J. Zhu, F. Meng, X. Song and Z. Sun, *Superlattices Microstruct.*, 2011, 50, 98-106.
54. G. Hodes, *J. Phys. Chem. C*, 2008, 112, 17778-17787.
55. J. Zhang, F.-X. Xiao, G. Xiao and B. Liu, *New J. Chem.*, 2015, 39, 279-286.
56. E. áToby Kelsey, *J. Mater. Chem.*, 1997, 7, 563-568.
57. N. Murakami, Y. Kurihara, T. Tsubota and T. Ohno, *J. Phys. Chem. C*, 2009, 113, 3062-3069.
58. T. Tachikawa, S. Yamashita and T. Majima, *J. Am. Chem. Soc.*, 2011, 133, 7197-7204.
59. J. Yu, J. Low, W. Xiao, P. Zhou and M. Jaroniec, *J. Am. Chem. Soc.*, 2014, 136, 8839-8842.

Table titles:

Table 1. Mean size of CdS particles and optical band gap of the samples.

Cyclic time	Mean size of CdS particles (nm)	Optical band gap (eV)
0	–	3.21
3	15.5	3.19
5	9.6	3.19
7	22.6	3.18
9	26.3	3.16

Table 2. Elemental content of {101}, {001} facets for CdS/TNS unannealed and annealed at 500□, respectivly.

	Unannealed		Annealed	
	Cd (wt%)	F (wt%)	Cd (wt%)	F (wt%)
(101)	1.13	5.76	1.29	2.55
(001)	0.61	5.73	1.77	2.62

Figure captions:

Fig. 1. XRD patterns of CdS/TNS prepared with different SILAR cycles: (a) 0 cycles, (b) 3 cycles, (c) 5 cycles, (d) 7 cycles, and (e) 9 cycles.

Fig. 2. SEM images of CdS/TNS prepared with different SILAR cycles: (a) 0 cycles, (c) 3 cycles, (d) 5 cycles, (e) 7 cycles, (f) 9 cycles, and (b) a cross-section view.

Fig. 3. The SEM images for the CdS loaded TNS unannealed (a) and annealed at 500□ for 2h (b). (c) and (d) are the EDS spectra of the (101), (001)facets for unannealed TNS; (e) and (f) are the EDS spectra of the {101}, {001}facets for annealed TNS labelled with block diagram, respectively.

Fig. 4. (a) TEM image and (b) HRTEM image of CdS/TNS. The inset is a SAED pattern of the anatase single crystal nanosheet.

Fig. 5. XPS spectra (a) survey spectra, (b) F 1s, (c) O 1s, (d) Ti 2p, (e) S 2p, (f) Cd 3d for the CdS/TNS unannealed and annealed at 500□ for 2h

Fig. 6. UV-Visible absorption spectra of CdS/TNS prepared with different SILAR cycles.

Fig. 7. Plot of $(\alpha h\nu)^2$ vs photon energy for CdS/TNS prepared with different SILAR cycles: (a) 0 cycles, (b) 3 cycles, (c) 5 cycles, (d) 7 cycles, and (e) 9 cycles.

Fig. 8. PL spectra of CdS/TNS prepared with different SILAR cycles.

Fig. 9. Photocurrent transients of CdS/TNS prepared with different SILAR cycles.

Fig. 10. Schematic diagram of charge separation among different crystal faces and CdS particles.

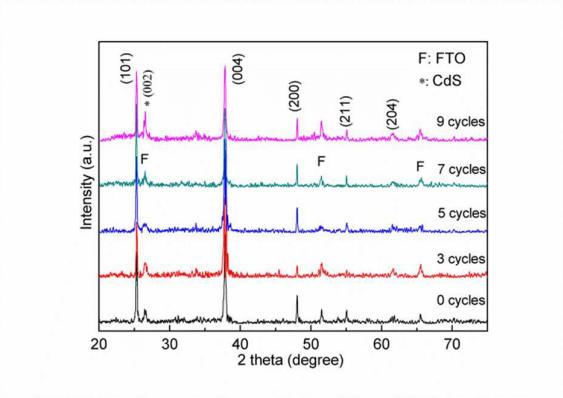

Fig. 1. XRD patterns of CdS/TNS prepared with different SILAR cycles: (a) 0 cycles, (b) 3 cycles, (c) 5 cycles, (d) 7 cycles, and (e) 9 cycles.

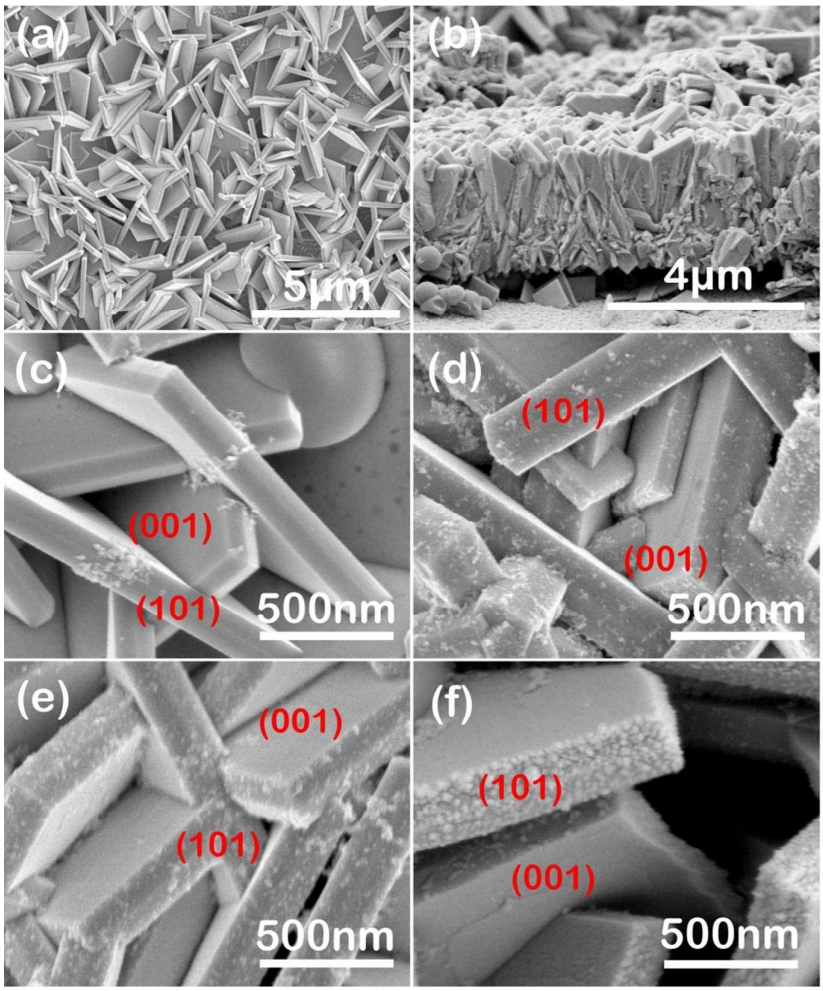

Fig. 2. SEM images of CdS/TNS prepared with different SILAR cycles: (a) 0 cycles, (c) 3 cycles, (d) 5 cycles, (e) 7 cycles, (f) 9 cycles, and (b) a cross-section view.

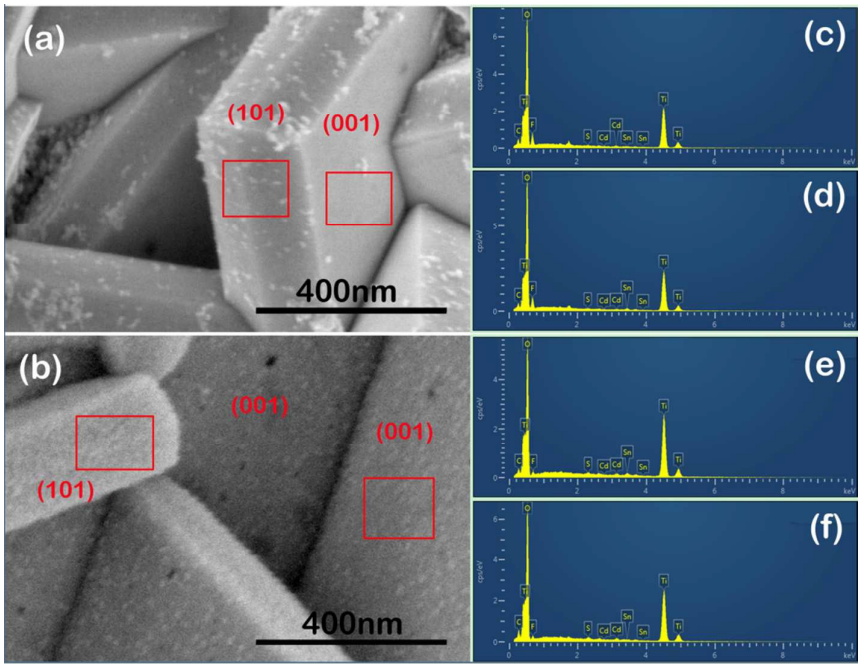

Fig. 3. The SEM images for the CdS/TNS unannealed (a) and annealed at 500□ for 2h (b). (c) and (d) are the EDS spectra of the (101), (001)facets for unannealed TNS, (e) and (f) are the EDS spectra of the (101), (001)facets for annealed TNS labelled with red block diagram, respectively.

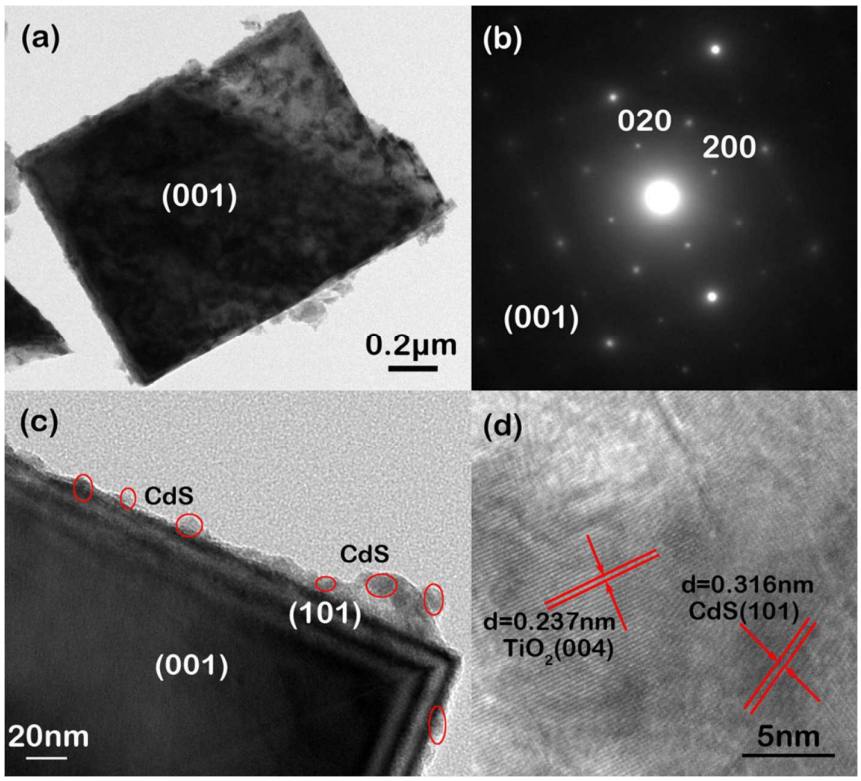

Fig. 4. (a), (c) TEM images and (d) HRTEM image of CdS/TNS. (b) SAED pattern of the anatase single crystal nanosheet.

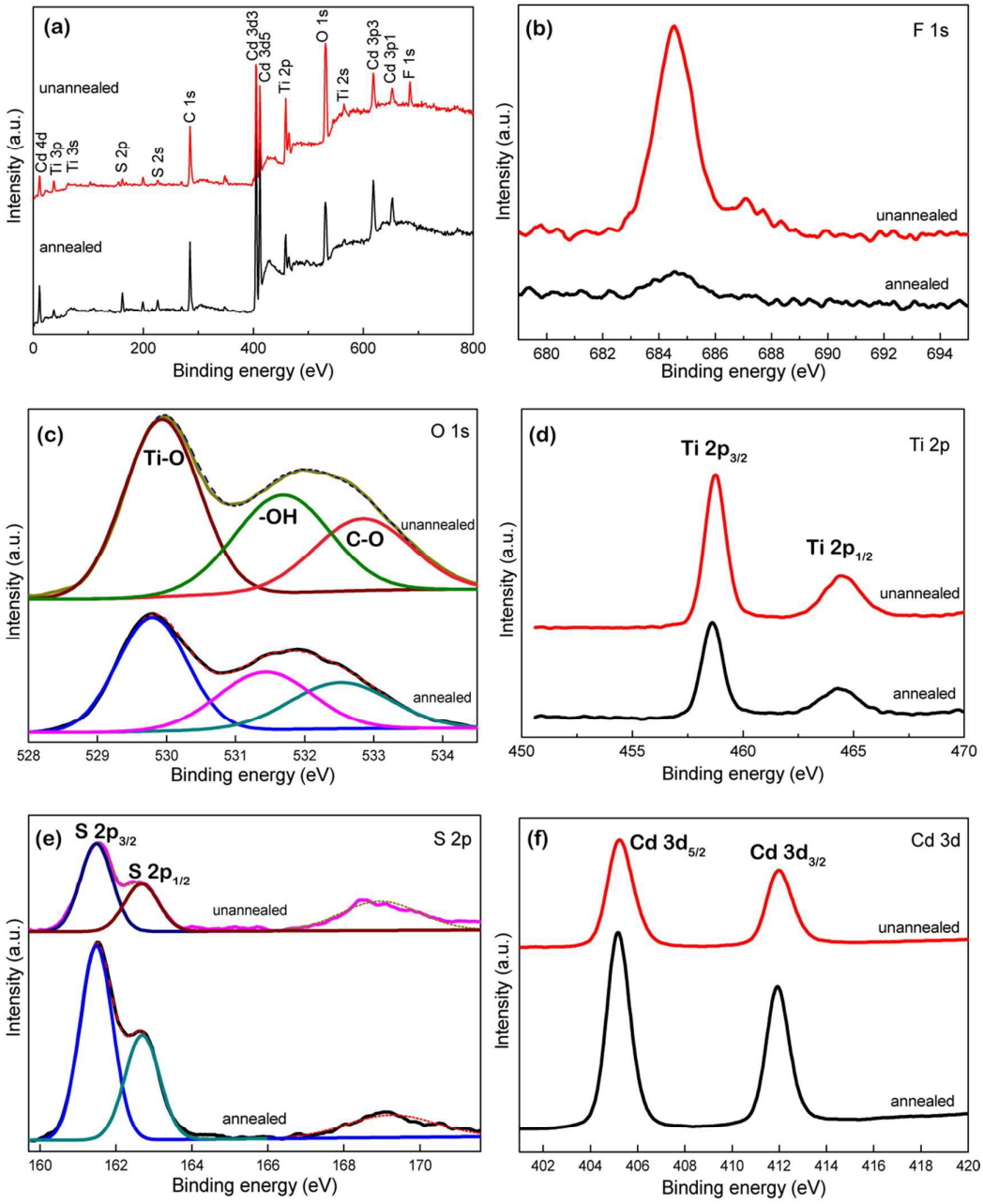

Fig. 5. XPS spectra (a) survey spectra, (b) F 1s, (c) O 1s, (d) Ti 2p, (e) S 2p, (f) Cd 3d for the CdS/TNS unannealed and annealed at 500□ for 2h

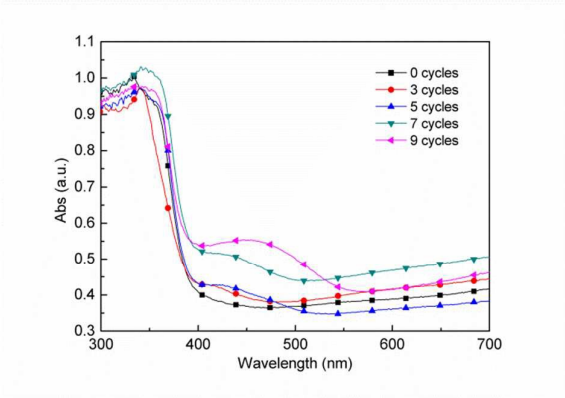

Fig. 6. UV-Visible absorption spectra of CdS/TNS prepared with different SILAR cycles.

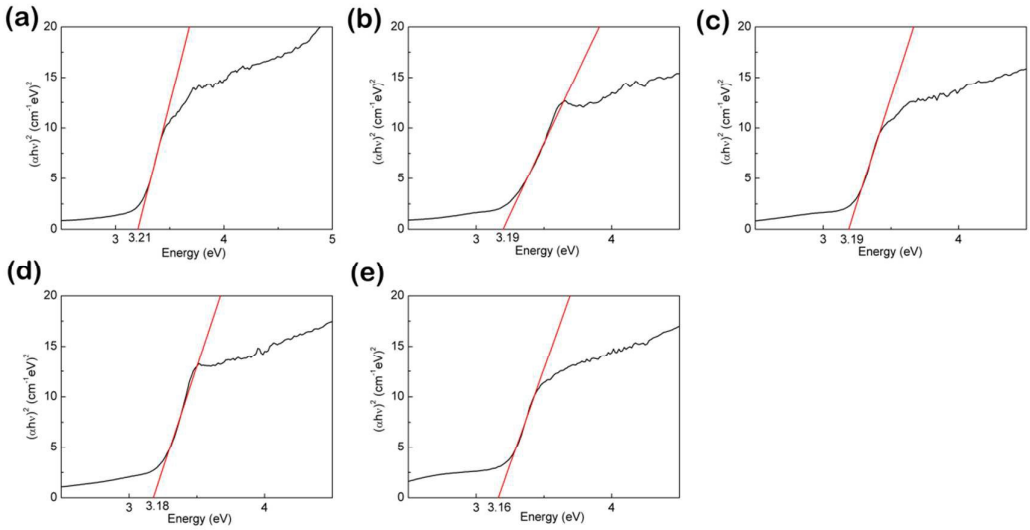

Fig. 7. Plot of $(\alpha h\nu)^2$ vs photon energy for CdS/TNS prepared with different SILAR cycles: (a) 0 cycles, (b) 3 cycles, (c) 5 cycles, (d) 7 cycles, and (e) 9 cycles.

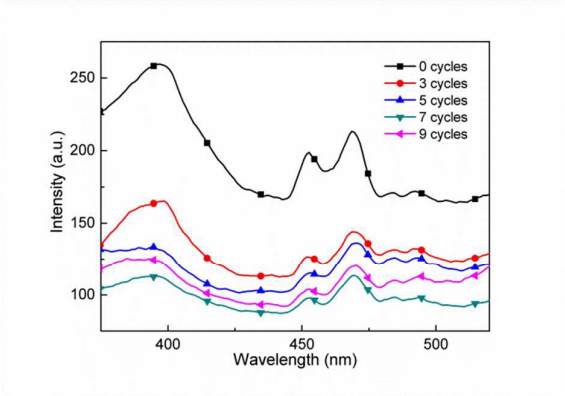

Fig. 8. PL spectra of CdS/TNS prepared with different SILAR cycles.

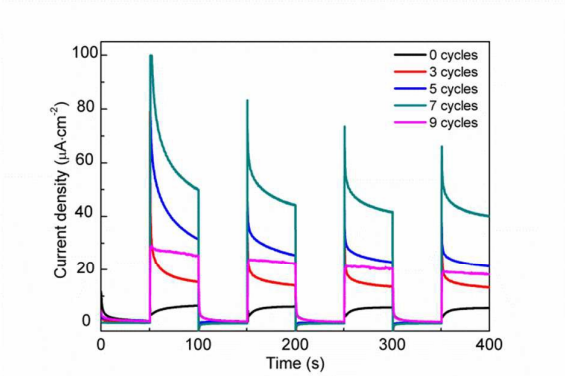

Fig. 9. Photocurrent transients of CdS/TNS prepared with different SILAR cycles.

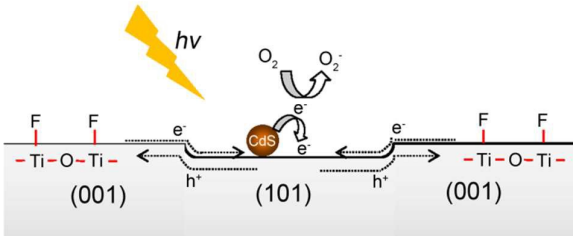

720

721 Fig. 10. Schematic diagram of charge separation among different crystal faces and CdS particle.

722

723

The selective deposition of CdS nanoparticles on the {101} facets of TiO_2 nanosheets combines with synergistic effect of {001} and {101} facets, enhance the spatial separation of electrons and holes on different facets, thereby improving the photoelectronic performance.